Nuclear Physics A542 (1992) 310–340
North-Holland

NUCLEAR
PHYSICS A

Soft dipole excitations in ^{11}Li

H. Esbensen
Physics Division, Argonne National Laboratory, Argonne, IL 60439, USA

G.F. Bertsch
Cyclotron Laboratory, Michigan State University, East Lansing, MI 48824, USA

Received 22 October 1991
(Revised 6 January 1992)

Abstract: A three-body model of ^{11}Li is extended to include all interactions in unbound states in the continuum. We use a Green function technique to solve the three-body hamiltonian equation, and study the continuum dipole states produced by electromagnetic excitations of the ground state. The final-state interaction modifies the dipole strength function substantially, making it similar to an independent-particle strength function, but the total strength is enhanced by 50% due to ground-state correlations. The dipole strength is concentrated in a peak just above threshold, and the strength distribution is consistent with the measured beam energy dependence of the Coulomb dissociation cross section. This threshold peak also gives a narrow component in the neutron and the residual nucleus momentum distributions. The angular distributions of the neutrons emitted in Coulomb-induced reactions show a surprising anticorrelation, favoring emission with a large opening angle between the directions of the two neutrons in the rest frame of ^{11}Li.

1. Introduction

The nucleus ^{11}Li is unique in having the smallest two-particle separation energy, and its properties are very much influenced by the large spatial distribution associated with the nearly unbound valence neutrons. In the last two years, the experimental study of this nucleus has burgeoned, following the work of Tanihata and coworkers using beams of ^{11}Li nuclei [1-5]). In a previous theoretical study [6]), we calculated the properties of the ground state of this nucleus in a three-body model consisting of the two valence neutrons and the ^{9}Li core, which we assumed to be inert. This model may be contrasted with the full shell-model approach [7,8]), which does not require an inert core, but on the other hand has difficulty with the large extension of the weakly bound neutrons. It may also be contrasted with a dineutron cluster model [9,10]), which is much simpler but limited in predictive power. Finally we mention three other three-body approaches besides the Green function technique we used, namely the variational method [11]), the Fadeev equations [12]), and the hyperspherical harmonic method [13]).

Correspondence to: Dr. H. Esbensen, Physics Division, Argonne National Laboratory, Argonne, IL 60439, USA.

Our model was successful in that the weak binding could be understood with a hamiltonian that was determined completely externally, i.e. with parameters fixed by the properties of other nuclei and by the free nucleon-nucleon interaction. Besides the energy of the nucleus, we also investigated the dipole excitations. These are strongly enhanced because the wave function extends out so far. Our calculation was less satisfactory here because we did not include the interaction in the final state. This produced a violation of the energy-weighted sum rule, and the shape of the strength function was much more spread out than in the independent-particle model.

In this paper we show how to generalize our Green function method to treat states in the continuum, thus allowing a consistent description of excited as well as ground states. This is applied to the dipole excitations, allowing us to calculate all properties of the final state. As we shall see, it is important to include the neutron-neutron interaction consistently in the ground state and in the excited states to describe the strength of the excitation as well as its concentration below 1 MeV excitation energy.

2. Two-particle model hamiltonian

In a previous study [6]) we introduced a simple model hamiltonian for nuclei (Z, A) which consists of two valence neutrons interacting with an inert core. We shall use exactly the same model in the present paper and we only summarize the basic ingredients here. We focussed on the effect of correlations between the valence neutrons, and used the following schematic hamiltonian,

$$H_2(\boldsymbol{r}_1, \boldsymbol{r}_2) = H_1(\boldsymbol{r}_1) + H_1(\boldsymbol{r}_2) + v(\boldsymbol{r}_1, \boldsymbol{r}_2)\,, \tag{2.1}$$

Here H_1 is the single-particle hamiltonian for a neutron interacting with the core, and $v(\boldsymbol{r}_1, \boldsymbol{r}_2)$ is an effective interaction between the two valence neutrons. Such a model hamiltonian is most realistic for loosely bound valence neutrons. For more tightly bound nuclei, as for example ^{16}O, correlations with the core nucleons will become more important.

The single-particle hamiltonian for the valence neutrons is parameterized in the usual way, with a kinetic energy operator, a Woods-Saxon potential and a spin-orbit interaction,

$$U(r) = V\left(\left(1 - 0.44 r_0^2 (\boldsymbol{l}\cdot\boldsymbol{s})\frac{1}{r}\frac{\mathrm{d}}{\mathrm{d}r}\right)\left(1 + \exp\left(\frac{r-R}{a}\right)\right)^{-1}\right), \tag{2.2}$$

with $a = 0.67$ fm, $R = r_0(A-2)^{1/3}$, and $r_0 = 1.27$ fm. The depth is adjusted so that the one-neutron separation energy of the $(Z, A-1)$ system is reproduced. In the case of ^{10}Li it is adjusted to produce a $p_{1/2}$ resonance at +0.8 MeV, which is achieved for $V = -30.2$ MeV.

The effective pair interaction is parameterized as a density-dependent contact interaction,

$$v(r_1, r_2) = \delta(r_1 - r_2)\left(v_0 + v_\rho\left(\frac{\rho_c(\frac{1}{2}(r_1, r_2))}{\rho_0}\right)^P\right), \tag{2.3}$$

where ρ_c is the matter density of the core and $\rho_0 = 0.16\,\mathrm{fm}^{-3}$. The density of the core was obtained by determining the wave functions of the core states using a single-particle hamiltonian of the form (2.2). Reasonable core states were obtained using the potential strength $V = -52 + 33((N-Z)/A)\tau_3$, supplemented for protons with a Coulomb interaction with the other $(Z-1)$ protons.

A zero-range interaction can only be meaningful in a truncated space. We have used the energy cutoff, $E_c = 40$ MeV, in the spectrum of two-particle states when we determine the eigenvalues of the hamiltonian (2.1). In order to make the interaction realistic outside the core, we adjust the strength v_0 to produce a large (actually infinite) scattering length. An infinite scattering length implies that the isolated two-neutron system has a bound state at zero energy. Using an energy cutoff of 40 MeV, this is achieved for

$$v_0 = -2\pi^2\left(\frac{\hbar^2}{m}\right)^{3/2} E_c^{-1/2} = -831\ \mathrm{MeV}\cdot\mathrm{fm}^3. \tag{2.4}$$

The parameters v_ρ and P for the density-dependent part of the interaction were adjusted so that the calculated two-neutron separation energies for ^{12}Be and ^{14}C reproduce the measured values. The calculational technique is described in detail in ref. [6]). The extracted values ($v_\rho = 930\ \mathrm{MeV}\cdot\mathrm{fm}^3$, $P = 1.2$) imply that the effective interaction essentially vanishes inside the core.

The two-particle hamiltonian (2.1) was used in ref. [6]) primarily to study ground-state properties of ^{11}Li but also of other neutron-rich nuclei. We found that ^{11}Li is bound with a two-neutron separation energy of $S_{2n} = 0.20$ MeV, which is not unreasonable in comparison to experimental values. We shall in the following use exactly the same hamiltonian interaction to calculate the correlated dipole response of ^{11}Li and the angular distribution of the emitted neutrons.

3. Correlated dipole response

We shall formulate the problem the same as we did earlier [6]), to calculate the response of the system to some operator. The ground state was calculated from the response to the two-neutron pair addition operator, which involves the construction of the two-particle Green function for the total angular momentum $J = 0$. The lowest pole in this response function determines the energy of the ground state, and the associated wave function can be found from the orbital dependence of the Green function at the pole.

In our previous work, we neglected the interaction between the two neutrons in excited states and calculated the dipole response by evaluating the matrix elements

$$M^{(0)}(\mathrm{E1}) = \langle (j_1 j_2)^1_\mu | D_\mu(r_1, r_2) | \Psi_{\mathrm{g.s.}} \rangle . \tag{3.1}$$

Here $\Psi_{\mathrm{g.s.}}$ is the correlated ground state of the two valence neutrons, and

$$D_\mu(r_1, r_2) = -\frac{Ze}{A}(r_1 Y_{1\mu}(\hat{r}_1) + r_2 Y_{1\mu}(\hat{r}_2)) \tag{3.2}$$

is the effective dipole operator. The noninteracting final states $(j_1 j_2)^1_\mu$ are obtained by coupling two independent-particle states, $(k_1 l_1 j_1)$ and $(k_2 l_2 j_2)$ with energies e_1 and e_2, to a state with total angular momentum $J = 1$,

$$|(j_1 j_2)^1_\mu\rangle = \sum_{m_1 m_2} \langle j_1 m_1 j_2 m_2 | 1\mu \rangle \psi_{k_1 l_1 j_1 m_1}(r_1) \psi_{k_2 l_2 j_2 m_2}(r_2) . \tag{3.3}$$

Detailed expressions for the dipole matrix elements are given in appendix D of ref. [6]) in terms of the single-particle wave functions.

The dipole strength distribution can be expressed in terms of the two-particle Green function $G(E)$ for $J = 1$ final states,

$$\begin{aligned} \frac{\mathrm{d}B(\mathrm{E1})}{\mathrm{d}E} &= \frac{1}{\pi} \operatorname{Im} \sum_\mu \langle \Psi_{\mathrm{g.s.}} | D^*_\mu G(E) D_\mu | \Psi_{\mathrm{g.s.}} \rangle \\ &= \frac{1}{\pi} \operatorname{Im} \sum_\mu \int \mathrm{d}r_1 \, \mathrm{d}r_2 \, \mathrm{d}r'_1 \, \mathrm{d}r'_2 \\ &\quad \times \Psi^*_{\mathrm{g.s.}}(r_1, r_2) D^*_\mu(r_1, r_2) G(E, r_1, r_2, r'_1, r'_2) D_\mu(r'_1, r'_2) \Psi_{\mathrm{g.s.}}(r'_1, r'_2) . \end{aligned} \tag{3.4}$$

Our earlier approach [6]), using eq. (3.1), is equivalent to eq. (3.4) using the non-interacting two-particle Green functions

$$G(E) = \sum_{\mu, \mathrm{f.st.}} \frac{|(j_1 j_2)^1_\mu\rangle\langle(j_1 j_2)^1_\mu|}{e_1 + e_2 - E - i\eta} , \tag{3.5}$$

where the sum over final states (f.st.) includes all independent two-particles states of the form given in eq. (3.3). Note that the variable E represents the two-particle energy of the excited state.

We can now include the effect of the interaction in excited states into the response. This will be done in the Tamm-Dancoff approximation, replacing the two-particle Green function in eq. (3.4) by

$$\begin{aligned} G_{\mathrm{TDA}}(E) &= (1 + G(E)v)^{-1} G(E) \\ &= G(E) - G(E)v(1 + G(E)v)^{-1} G(E) . \end{aligned} \tag{3.6}$$

The second equality shows that the TDA response can be written as the uncorrelated

response minus a correction term,

$$\frac{dB(E1)}{dE} = \frac{1}{\pi} \operatorname{Im} \sum_{\mu} \langle \Psi_{g.s.} | D_{\mu}^{*} G(E) D_{\mu} | \Psi_{g.s.} \rangle$$

$$- \frac{1}{\pi} \operatorname{Im} \sum_{\mu} \langle \Psi_{g.s.} | D_{\mu}^{*} G(E) v (1 + G(E) v)^{-1} G(E) D_{\mu} | \Psi_{g.s.} \rangle . \quad (3.7)$$

The validity of this expression is verified in subsect. 3.1. The correction term in eq. (3.7) is not too hard to calculate when we use a contact interaction for the pairing field. This is discussed in subsect. 3.2.

3.1. DIPOLE MATRIX ELEMENTS

We shall now give a more detailed derivation of eq. (3.7) and calculate the dipole matrix element to a specific two-particle final state. The result will be particularly important for the calculation of angular distributions of the emitted neutrons. The effect of the pair interaction in excited states can be considered as a rescattering of the two neutrons after they have been excited by the dipole field. Making use of the non-interacting two-particle Green function, eq. (3.5), evaluated at a fixed two-particle energy $E = e_1 + e_2$, we can in fact perform the summation of the scattering series, and express the result in a closed form. Thus we obtain the dipole matrix element

$$M(E1) = \langle (j_1 j_2)^{1}_{\mu} | (1 + v G(E))^{-1} D_{\mu}(r_1, r_2) | \Psi_{g.s.} \rangle . \quad (3.8)$$

Summing over all final states (f.st.) we obtain the following expression for the dipole strength distribution

$$\frac{dB(E1)}{dE} = \sum_{\mu, f.st.} |M(E1)|^2 \delta(E - e_1 - e_2)$$

$$= \frac{1}{\pi} \sum_{\mu} \langle \Psi_{g.s.} | D_{\mu}^{*} (1 + G^{+}(E) v)^{-1} \operatorname{Im} (G(E))$$

$$\times (1 + v G(E))^{-1} D_{\mu} | \Psi_{g.s.} \rangle . \quad (3.9)$$

One can show that this expression is identical to the TDA expression for the response, eq. (3.7).

From the dipole matrix elements one can also construct a more detailed strength distribution, namely as a differential in the kinetic energy of the two emitted neutrons,

$$\frac{d^2 B(E1)}{de_1 \, de_2} = 3 \sum_{l_1 j_1 l_2 j_2} |M(E1)|^2 \frac{dk_1}{de_1} \frac{dk_2}{de_2} , \quad (3.10)$$

which we shall illustrate in sect. 4. The factors dk/de originate from the normalization of the continuum single-particle wave functions that we have chosen (see eq. (A.3));

the dipole matrix elements are independent of μ and the factor of 3 comes from the three possible μ-values.

3.2. TECHNICAL DETAILS OF NUMERICAL CALCULATIONS

We shall now describe in more detail how one can calculate the corrections to the dipole strength and the dipole matrix elements that are due to the interaction between the two neutrons in excited states. The correction to the dipole strength is given by the second term in eq. (3.7), whereas the correction to the dipole matrix element is (cf. eqs. (3.1) and (3.8))

$$\begin{aligned}\Delta M(\mathrm{E1}) &= M(\mathrm{E1}) - M^{(0)}(\mathrm{E1}) \\ &= -\langle (j_1 j_2)^1_\mu | v(1+G(E)v)^{-1} G(E) D_\mu(\boldsymbol{r}_1, \boldsymbol{r}_2) | \Psi_{\mathrm{g.s.}} \rangle . \end{aligned} \tag{3.11}$$

First we note that eqs. (3.7) and (3.11) contain the operator $v(1+G(E)v)^{-1}$. To construct this operator we only need the two-particle Green function at identical positions of the two neutrons (i.e. $\boldsymbol{r}_1 = \boldsymbol{r}_2$ and $\boldsymbol{r}_1' = \boldsymbol{r}_2'$), since we have assumed that the pairing field is a contact interaction. This is a very important simplification, without which the calculation would become impractical.

Secondly, we note that the noninteracting Green function, eq. (3.5), is determined by a sum over ($J = 1$) two-particle states in the continuum. In ref. [6]) we calculated the correlated ground state ($J = 0$) by discretizing the continuum. If we used the same method to calculate the dipole response we would obtain unphysical structures in the response due to the discrete nature of the single-particle spectrum. We shall therefore use a different method and perform the sum over true continuum states. The imaginary part of the Green function causes no problem. The real part is more difficult. This we obtain from the Kramers-Kronig dispersion relation to the imaginary part, using a Gauss-Legendre integration technique. The construction of the noninteracting Green function, for identical positions of the two neutrons, is described in appendix A.

We can now write the correction (3.11) to the dipole matrix elements as

$$\begin{aligned}\Delta M(\mathrm{E1}) = -(-1)^{l_1} \sqrt{\frac{2j_1+1}{8\pi}} \langle j_1 \tfrac{1}{2} 10 | j_2 \tfrac{1}{2} \rangle \int \mathrm{d}\boldsymbol{r} \int \mathrm{d}\boldsymbol{r}' \, \phi_{k_1 l_1 j_1}(r) \phi_{k_2 l_2 j_2}(r) \\ \times Y^*_{1\mu}(\hat{\boldsymbol{r}}) v(r) (1+G(E)v)^{-1}_{r,r'} G_D(E, \boldsymbol{r}') , \end{aligned} \tag{3.12}$$

where we have inserted eq. (A.11) of ref. [6]) for the final state, and introduced the function

$$G_D(E, \boldsymbol{r}) = \int \mathrm{d}\boldsymbol{r}_1 \int \mathrm{d}\boldsymbol{r}_2 \, G(E, \boldsymbol{r}, \boldsymbol{r}, \boldsymbol{r}_1, \boldsymbol{r}_2) D_\mu(\boldsymbol{r}_1, \boldsymbol{r}_2) \Psi_{\mathrm{g.s.}}(\boldsymbol{r}_1, \boldsymbol{r}_2) . \tag{3.13}$$

The numerical calculation of G_D is described in appendix B. Note that the first two coordinates in the argument of the two-particle Green function are identical in eq.

(3.13). This is again a consequence of the assumption that the pairing field is a contact interaction.

From eq. (B.1) we see that the integration in eq. (3.12) over the orientations of $\hat{r}$ and $\hat{r}'$ only involves

$$\int \mathrm{d}\hat{r} \int \mathrm{d}\hat{r}'\, Y^*_{1\mu}(\hat{r})(1+G(E)v)^{-1}_{r,r'} Y_{1\mu}(\hat{r}') = (1+G(E)v)^{-1}_{r,r'}. \tag{3.14}$$

It is therefore sufficient to invert the radial part of the operator $(1+G(E)v)$, which can be done in the usual way on a finite radial grid [see ref. [14])].

The function $G_D(E, r)$, defined in eq. (3.13) and discussed in appendix B, can also be used to calculate the correction to the dipole strength which is due to the interaction between the two neutrons in excited states. Thus we obtain (cf. eq. (3.7))

$$\frac{\mathrm{d}B(\mathrm{E1})}{\mathrm{d}E} = \frac{1}{\pi}\,\mathrm{Im}\sum_{\mu}\langle\Psi_{\mathrm{g.s.}}|\mathrm{D}^*_{\mu}\mathrm{G(E)D}_{\mu}|\Psi_{\mathrm{g.s.}}\rangle - \frac{1}{\pi}\,\mathrm{Im}\sum_{\mu}\int r^2\,\mathrm{d}r\int r'^2\,\mathrm{d}r'$$
$$\times G_D(E, r)v(r)(1+G(E)v)^{-1}_{r,r'}G_D(E, r'). \tag{3.15}$$

Let us finally mention that the method outlined above, to calculate the correlated two-particle Green function from true continuum single-particle wave functions making use of the dispersion relation, can also be used to construct the response for other multipolarities. It can easily be supplemented with contributions from bound, single-particle states if such exist (in the case of ^{11}Li all the relevant states belong to the continuum since ^{10}Li is unbound). In particular, this method can also be used to determine the correlated ground state of the two valence neutrons. In the present work we shall, however, use the correlated ground state of ^{11}Li that we have determined previously [6]) from discretizing the continuum in a large box, as the initial state for the dipole response. Thus the treatments of initial and final states are in principal different but we do not expect that this difference will cause any serious inconsistency in our calculations of the dipole response.

The correlated ground state of ^{11}Li was calculated on a radial grid as described in ref. [6]), and the calculation converged quite well for $r_{\max} = 40$ fm and a step size of 0.25 fm. The dipole response to noninteracting final states has also converged for this choice and it is sufficient to include single-particle states with orbital angular momenta up to $l_{\max} = 10$. It is numerically much more difficult to include the effect of the pair interaction in the final state, in particular at low excitations. The problem is the calculation of the operator (3.14) which governs the dynamical evolution of the two excited neutrons. To construct this operator we included all partial waves up to $l_{\max} = 20$ and performed the Gauss-Legendre integration (A.4), (A.6), (A.7) with up to 20 points. The calculated response converged in this case for excitations larger than 0.5 MeV. The trend of our calculations seems to indicate that a more accurate calculation might shift the position of the maximum response even closer to threshold (see fig. 1 in the next section). At present, we do not want to improve the accuracy of our calculations since it would be very time consuming. Moreover,

the uncertainties in our results at very low excitations are probably insignificant when comparing to measurements.

4. Results on the strength function and Coulomb dissociation

The correlated dipole response of the valence neutrons in ^{11}Li, calculated as described in the previous section, is shown by the fully drawn curve in fig. 1. The parameters for the calculation, i.e. the single-particle hamiltonian and the pair-interaction, are the same as those used in ref. [6]). To interpret this result, it is useful to compare with the predictions of simpler models. The dot-dashed curve shows the response obtained in our earlier work by neglecting the effect of the pair-interaction in the final state. We see that this is not a very good approximation for the case at hand. It predicts more strength at higher energies; the effect of the final state interaction is to shift the maximum in the strength much closer to the threshold at $\Delta E = -\varepsilon_{g.s.} = 0.2$ MeV. We have also calculated the distribution assuming plane wave final states, and find a distribution very similar to the dot-dashed curve.

It is also interesting to compare the strength distribution to that obtained from the independent-particle model, because that model is so easy to apply. Here one takes the initial and final neutron wave functions as eigenfunctions of some single-particle potential. There is of course some uncertainty in the choice of the parameters

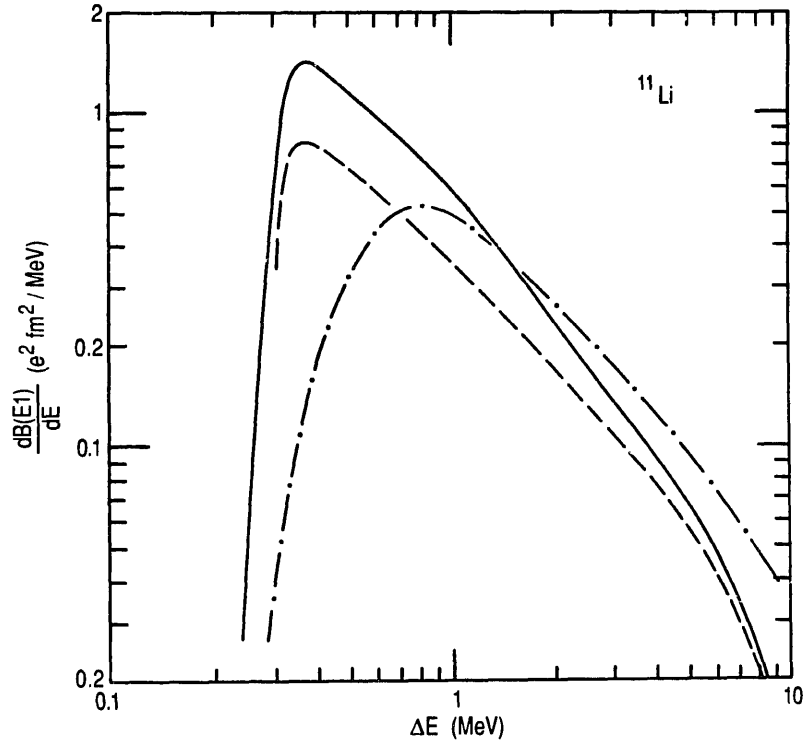

Fig. 1. Dipole strength of the valence neutrons in ^{11}Li as a function of the excitation energy. The solid curve is the correlated response. The dot-dashed curve was obtained by ignoring the pair-interaction in the final state. The dashed curve is the independent particle response obtained as explained in the text.

for the potential well. We have chosen a model which reproduces the single-neutron density obtained from the correlated ground state (see sect. 5 of ref. [6])). In order to reproduce this density it was necessary to increase the core radius by 20% and adjust the depth of the single-particle potential accordingly. The best fit was obtained for a $p_{1/2}$ single-particle state with a binding energy of 0.3 MeV. The associated dipole response is shown by the dashed curve in fig. 1. The shape is remarkably similar to that of the correlated response at excitation energies smaller than 1 MeV. The total strength, however, is smaller.

One can understand some of the main features of the above four models of the response by considering different sum rules. The first sum is the total $B(\mathrm{E1})$ strength, which has the value $B(\mathrm{E1}) = 1.57\, e^2\,\mathrm{fm}^2$ in the fully correlated model. It has the same value when the neutron–neutron interaction is neglected in the final states, a slightly higher value for the plane-wave final states, and a much smaller value for the independent-particle model, $B(\mathrm{E1}) = 1.07\, e^2\,\mathrm{fm}^2$. The equality of the correlated responses is a consequence of the closure relation which can be used to calculate the total $B(\mathrm{E1})$ as an expectation value in the ground state,

$$B(\mathrm{E1}) = \int_{-\infty}^{+\infty} \mathrm{d}E \frac{\mathrm{d}B(\mathrm{E1})}{\mathrm{d}E} = \frac{3}{4\pi}\left(\frac{Ze}{A}\right)^2 \langle r_1^2 + r_2^2 + 2\boldsymbol{r}_1 \cdot \boldsymbol{r}_2 \rangle . \tag{4.1}$$

This is exact for the plane-wave model; for the other cases the actual strength is slightly smaller since the sum (4.1) includes forbidden transitions to occupied core states. We have already noted that the total strength of the independent-particle response (dashed curve) is smaller than that of the correlated response, although the independent-particle model has been adjusted to give the same single-particle density. The difference can be explained by the sum rule (4.1). The last term, $\langle 2\boldsymbol{r}_1 \cdot \boldsymbol{r}_2 \rangle$, which vanishes in the independent-particle model, enhances the total strength of the correlated response by 43%. It is also seen that the total strength would be enhanced by 100% if one assumes that the two valence neutrons form a point particle.

The energy-weighted sum of the two correlated responses are different. For the full response including the final state interaction, the total hamiltonian is the same in the initial and final state, and one can use the sum rule [6,15])

$$S_1 = \int_{-\infty}^{+\infty} \mathrm{d}E \frac{\mathrm{d}B(\mathrm{E1})}{\mathrm{d}E}(E - \varepsilon_{\mathrm{g.s.}}) = 2\frac{9}{4\pi}\left(\frac{Ze}{A}\right)^2 \frac{\hbar^2}{2m} = 2.2\, e^2\,\mathrm{fm}^2\,\mathrm{MeV}. \tag{4.2}$$

Again, this sum includes (negative) contributions from the forbidden transitions to occupied core states; the actual energy-weighted sum over allowed transitions increases from 2.2 to 3.2 $e^2\,\mathrm{fm}^2\mathrm{MeV}$. Neglecting the final-state interaction (dot-dashed curve in fig. 1) one obtains an even larger energy-weighted sum. This fact led us in ref. [6]) to the conclusion that the final-state interaction must have a significant effect on the dipole response. This is indeed confirmed by the comparison of the two responses (the fully drawn and dashed-dotted curves) shown in fig. 1.

The average energy of the $B(\mathrm{E1})$ strength function is an interesting quantity. We determine it easily from the sums in the above paragraph, finding

$$\langle \Delta E \rangle_B = S_1 / B(\mathrm{E1}) = 2.04 \text{ MeV}. \tag{4.3}$$

In ref. [15]) a value of 1.6 MeV was obtained using the same sum rules but a different description of the ground state. In the dineutron cluster model [10]) the average energy is given by

$$\frac{\int \mathrm{d}E\,(E-\varepsilon_{\mathrm{g.s.}})^{3/2}E^{-3}}{\int \mathrm{d}E\,(E-\varepsilon_{\mathrm{g.s.}})^{3/2}E^{-4}} = 6\varepsilon_{\mathrm{g.s.}} \simeq 1.5 \text{ MeV}. \tag{4.4}$$

From the similarity of these results we expect that the average energy is rather well determined theoretically, and it would be very surprising if the actual distribution turned out very different.

A contour plot of the double-differential strength function, depending on the individual energies of the two neutrons, is shown in fig. 2. Two interesting features are observed: a large concentration of strength at small final-state energies, and a ridge when the energy of one of the neutrons is large. The ridge appears at an energy of about 0.7 MeV. It reflects the physical process in which one of the neutrons is dipole-excited while the other remains as a spectator near the $p_{1/2}$ resonance in ^{10}Li. These features were already seen in fig. 11 of ref. [6]), where we showed the correlated dipole response obtained by neglecting the final state interaction.

In fig. 3 we show the corresponding predicted energy distribution assuming plane wave final states. The distribution is much smoother in this oversimplified model,

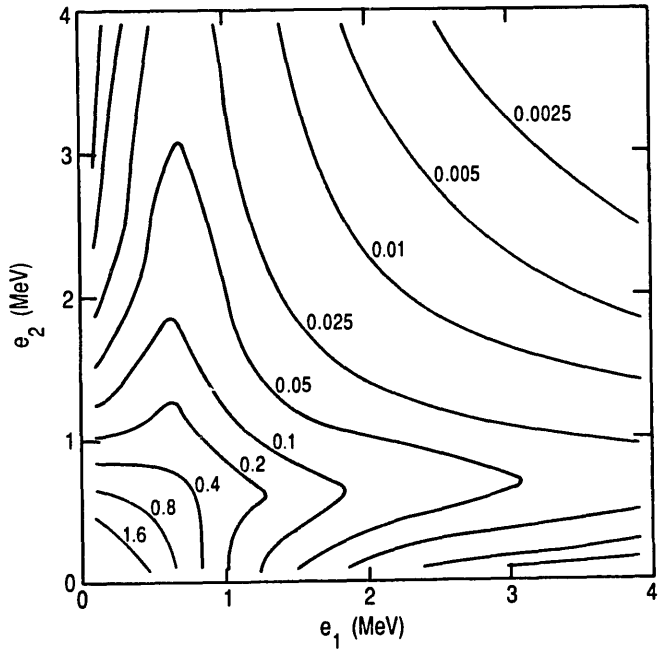

Fig. 2. Contour plot of the correlated dipole response of the valence neutrons in ^{11}Li, as a function of the energies of the two emitted neutrons. The contour values are in units of e^2 fm^2.

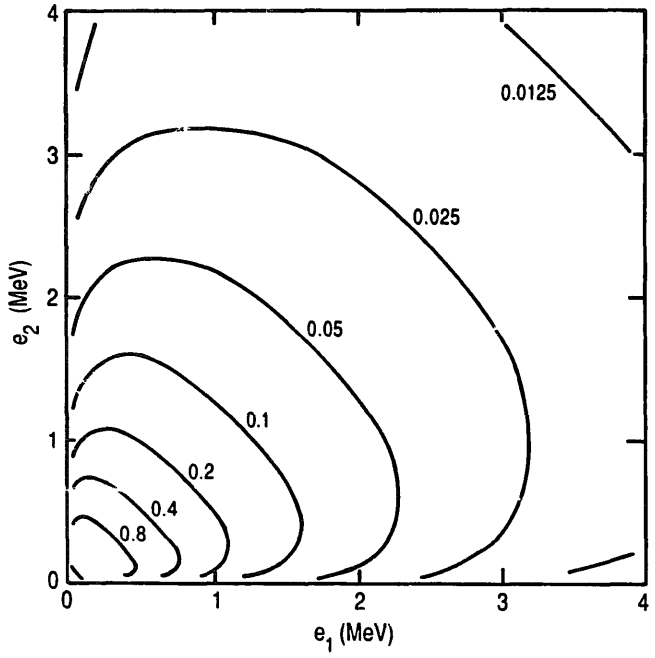

Fig. 3. Contour plot of the dipole response of the valence neutrons in ^{11}Li assuming plane-wave final states. The contour values are in units of e^2 fm^2.

and misses both the ridges from the single-particle resonance and the strong enhancement near threshold.

4.1. COULOMB DISSOCIATION

The dipole strength shown in fig. 2 is closely related to the differential cross section for the emission of the two neutrons, with energies e_1 and e_2 in the rest frame of ^{11}Li. The part of this cross section that is generated by the dipole component of the Coulomb field from a target nucleus is well known [16]) and can for example be obtained from the general formula (5.9), by inserting eqs. (5.11) and (5.13a, b),

$$\frac{\mathrm{d}^2\sigma^{\mathrm{Dip}}}{\mathrm{d}e_1\,\mathrm{d}e_2}=\left(\frac{4\pi Z_{\mathrm{T}}e}{3\hbar v}\right)^2\frac{\mathrm{d}^2B(\mathrm{E1})}{\mathrm{d}e_1\,\mathrm{d}e_2}L(\xi)\,, \tag{4.5}$$

where

$$L(\xi)=2\xi K_0(\xi)K_1(\xi)-\left(\frac{v}{c}\right)^2\xi^2(K_1^2(\xi)-K_0^2(\xi))\,, \tag{4.6}$$

and ξ is the adiabaticity parameter [see eq. (5.10)]. A detailed comparison to data requires, of course, additional information about the nuclear part of the cross section. Anyway, a direct comparison to data may be useful for reactions on a heavy target, where Coulomb dissociation constitutes a major part of the cross section. The cross section (4.5) is even more strongly peaked at low excitations than is the dipole

strength shown in fig. 2. This is clearly seen for small values of ξ, i.e. low excitations and/or large velocities, where the function $L(\xi)$ reduces to

$$L(\xi) \simeq 2 \log\left(\frac{1.123\hbar\gamma v}{\Delta E R_{\text{eff}}}\right) - \left(\frac{v}{c}\right)^2 . \tag{4.7}$$

Here we have inserted the expression (5.10) for ξ in terms of the excitation energy $\Delta E = e_1 + e_1 - \varepsilon_{\text{g.s.}}$.

Since the dipole strength of the valence neutrons in ^{11}Li is concentrated at very low excitations it is possible to give a simple parametrization of the corresponding Coulomb dissociation cross section. Integrating over all excitation energies we obtain from eq. (4.5), using the approximation (4.7), the following expression

$$\sigma^{\text{Dip}} = \left(\frac{4\pi Z_{\text{T}} e}{3\hbar v}\right)^2 B(\text{E1}) \left(2 \log\left(\frac{1.123\hbar\gamma v}{I_D R_{\text{eff}}}\right) - \left(\frac{v}{c}\right)^2\right). \tag{4.8}$$

It depends on the dipole response through the total strength B(E1) and an average (logarithmic) excitation energy I_D, which is determined by

$$\log(I_D) = \frac{1}{B(\text{E1})} \int_0^\infty \mathrm{d}E \frac{\mathrm{d}B(\text{E1})}{\mathrm{d}E} \log(\Delta E) . \tag{4.9}$$

We find for the average excitation energy the values $I_D = 1.56$ MeV and 1.33 MeV for the full response and the independent-particle model, respectively. Note that the Coulomb dissociation cross section (4.8) is primarily sensitive to the total dipole strength of the valence neutrons. The dependence on the logarithmic average energy is much weaker, particularly at high beam velocities.

The Coulomb dissociation cross section for (^{11}Li, ^{9}Li) reactions on a gold target is shown in fig. 4 as a function of the beam energy. The solid curve is the prediction from the fully correlated response. Numerically, this was obtained by integrating eq. (4.5), using the expression (4.6) for $L(\xi)$. The dotted curve is the corresponding result obtained from the analytic expression (4.8), which is seen to be quite accurate at beam energies larger than of 30 MeV/u. The parameters B(E1) and I_D have been quoted earlier. The "data points" were extracted by Sustich [17]) and by Bertsch *et al.* [18]) from the measurements by Anne *et al.* [4]) and Kobayashi *et al.* [3]), respectively; the latter was scaled from a lead to a gold target. The extracted values are model dependent so it is difficult to judge the quality of the agreement with the calculated cross sections. It would be useful to calculate the nuclear part of the fragmentation from the same correlated ground state that we have used to calculate the Coulomb dissociation.

Let us finally give an expression for the average excitation energy of the residual nucleus following Coulomb excitation, $\langle \Delta E \rangle_{\text{Cou}}$. We shall use this quantity to estimate the associated recoil momenta of the ^{9}Li fragment. If $L(\xi)$ were constant this would be the same as the first moment of the dipole strength distribution, $\langle \Delta E \rangle_B$.

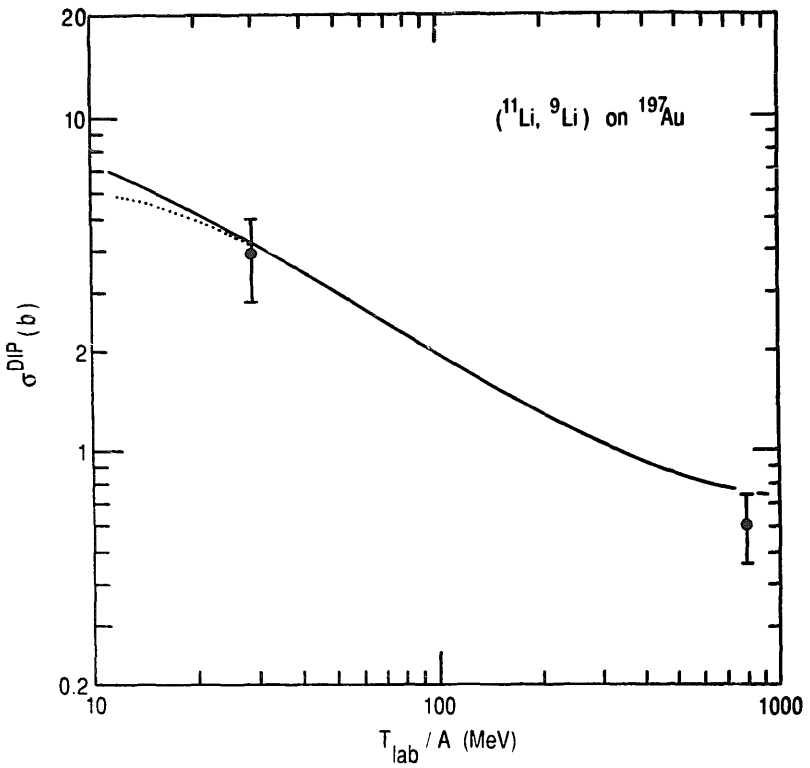

Fig. 4. Coulomb dissociation cross section for (^{11}Li, ^{9}Li) reactions on a gold target, as a function of the beam energy per nucleon. The solid curve was calculated from the correlated dipole response of the valence neutrons. The dotted curve at lower energies shows the result obtained from the simple parameterization (4.8).

We include the dependence of $L(\xi)$ using the approximation (4.7), which yields

$$\langle \Delta E \rangle_{Cou} = \langle \Delta E \rangle_B - \frac{2\langle \Delta E \log(\Delta E / I_D) \rangle_B}{2\log(1.123\hbar\gamma v / I_D R_{eff}) - (v/c)^2}. \tag{4.10}$$

Inserting values for the two moments we obtain

$$\langle \Delta E \rangle_{Cou} = 2.04 - \frac{3.4}{2\log(1.123\hbar\gamma v / I_D R_{eff}) - (v/c)^2}\ \text{MeV}. \tag{4.10'}$$

This expression is compared in fig. 5 to a more accurate calculation based on eqs. (4.5), (4.6). The average excitation energy of the final state is 1 MeV at a beam energy of 30 MeV/u, only half the value expected for asymptotically high beam energies. Note that these averages are much higher than the peak energy, which is only 375 keV.

4.2. EXPERIMENTAL DISTRIBUTIONS

So far no measurements have been made in enough detail to directly extract the information about the energy distribution of the dipole response. However, there are two experiments which have indirect information that we can compare with.

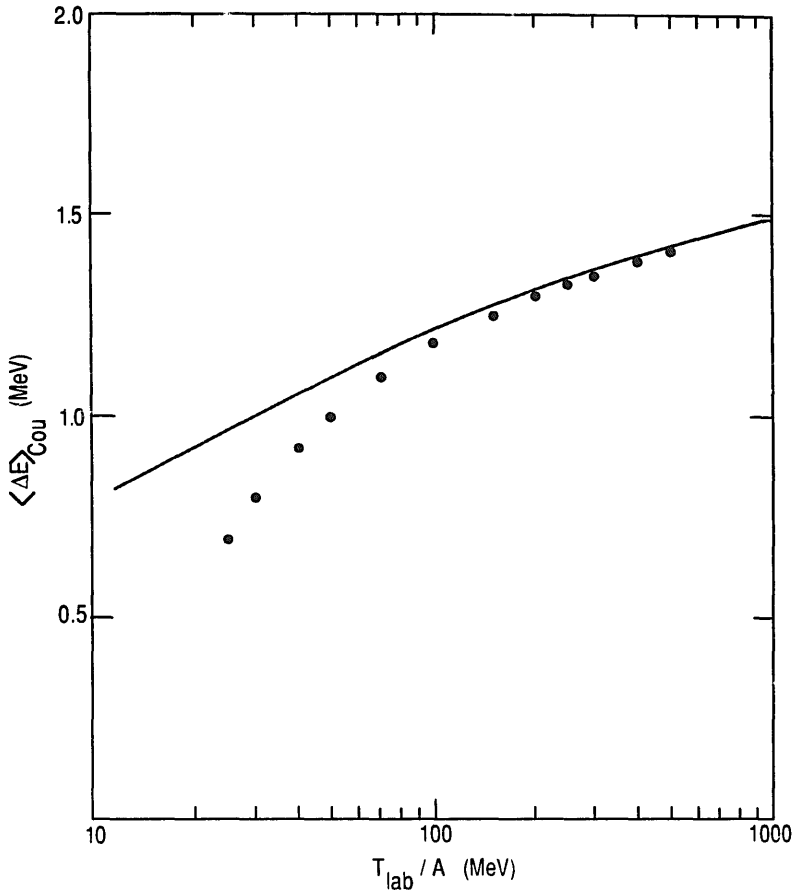

Fig. 5. Average Coulomb excitation energy in (^{11}Li, ^{9}Li) reactions on a gold target, as a function of the beam energy per nucleon. The dotted curve is the simple approximation (4.10), whereas the fully drawn curve is from a numerical integration of the dipole cross section (4.5), (4.6) times the excitation energy.

One experiment is the angular distribution of neutrons in the lab system, measured by Anne *et al.* [4]). They found that the distribution was very strongly forward peaked. The distribution was calculated by one of us using the independent particle model, finding good agreement with the data [19]). We want to make the following points here. First, the use of the independent-particle model for the shape of the dipole response seems to be well-justified by our comparison with the fully correlated model. A second point is that the neutron lab angular distribution is closely connected to the average energy of the excited state, provided the angular distribution in the frame of the ^{11}Li is nearly isotropic. We will examine the angular distribution in sect. 6, and show that it is expected to be nearly isotropic. The excitation energy is shared between the two neutrons and the mean square velocity of each neutron is given by

$$v_n^2 = (\langle \Delta E \rangle_{Cou} + \varepsilon_{g.s.})/m . \tag{4.11}$$

The transverse component is reduced by a factor of $\frac{2}{3}$, and from this we deduce the

mean square angle of the emitted neutrons in the lab frame,

$$\theta_n^2 = \frac{2v_n^2}{3v_{\text{beam}}^2} \simeq \frac{\langle \Delta E \rangle_{\text{Cou}} + \varepsilon_{\text{g.s.}}}{3E_{\text{beam}}} . \tag{4.12}$$

For the conditions of the experiment [4]) with $E_{\text{beam}} = 29$ MeV/u, the above equation yields $\theta_n = 5.4°$. The measured angular distributions have roughly the form $\exp(-\theta/\beta)$. From the estimate (4.12) we obtain the value $\beta = \sqrt{\frac{1}{6}}\,\theta_n = 2.2°$ for the slope parameter, which is in reasonable agreement with the data. One aspect of this measurement is puzzling, however. The width of the distribution is independent of target, although the excitation mechanism changes from mainly nuclear to mainly Coulomb as the target charge increases. On general grounds we expect the nuclear interaction to transfer more momentum to the neutrons and produce a more energetic final state spectrum than the dipole Coulomb field. Evidently, the difference is not enough to be visible in the experimental data.

The next observable we consider is the momentum distribution of the residual ^{9}Li nucleus. This has contributions from the recoil following neutron emission, and from the direct Coulomb and nuclear interactions with the target. The transverse momentum distribution was measured in ref. [2]), and a narrow component to the momentum distribution was seen for a low-Z target but not for a high-Z target. To make a prediction here, we must understand the angular correlation between the two neutrons, because the recoil is the vector sum from the neutrons. We shall find in sect. 6 that the neutron–neutron correlation can be safely neglected, because the two neutrons prefer to come out at right angles. Then the momentum recoil is given approximately by

$$\langle \Delta p^2 \rangle = 2m(\langle \Delta E \rangle_{\text{Cou}} + \varepsilon_{\text{g.s.}}) . \tag{4.13}$$

This yields 49 MeV/c, which is somewhat smaller than the 71 ± 15 MeV/c width observed on a lead target at 800 MeV/u. However, the transverse momentum imparted by the Coulomb deflection in the field of the target is not negligible. It is approximately

$$\Delta p \simeq \frac{2Z_P Z_T e^2}{vb} . \tag{4.14}$$

Estimating an average b of 24 fm, we find this contribution to be 35 MeV/c, which would account for the larger total. We have no explanation of the extremely narrow component found in the break-up on the light target. Coulomb effects (both deflection and dissociation) are expected to be insignificant in this case.

The problem of the additional momentum due to the Coulomb deflection is obviated if the longitudinal momentum of the ^{9}Li is measured instead of its transverse momentum. This quantity is the object of an experiment now in progress [20]), so we can expect more definitive information in the near future. For this observable, the actual shape of the momentum distribution might convey some useful information.

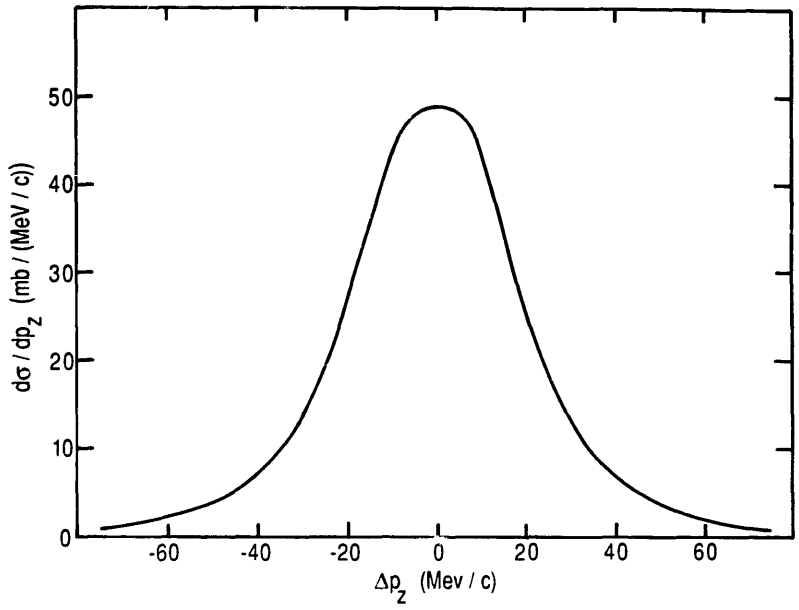

Fig. 6. Longitudinal recoil momentum distribution of ^{9}Li fragments, calculated as described in subsect. 4.2, for (^{11}Li, ^{9}Li) reactions on a gold target at a beam energy of 70 MeV/u.

We therefore evaluated the recoil distribution using the detailed excitation energy distribution from the fully correlated model. However, we keep our simplifying assumptions that the emission of neutrons is isotropic and without any angular correlation. For given momenta p_1 and p_2 of the two neutrons, the distribution with respect to momentum along the z-axis is

$$\frac{dn(p_z)}{dp_z} = \begin{cases} 0 & p_z > p_1 + p_2 \\ (p_1 + p_2 - p_z)/4p_1p_2 & p_1 + p_2 > p_z > |p_1 - p_2| \\ (p_1 + p_2 - |p_1 - p_2|)/4p_1p_2 & |p_1 - p_2| > p_z. \end{cases}$$

We convolute this with our predicted energy distribution, assuming the neutrons share the total energy with one getting $\frac{3}{4}$ and the other $\frac{1}{4}$ of the total. The results are shown in fig. 6 for a 70 MeV/u ^{11}Li beam on a gold target. The shape of the distribution is more peaked than a gaussian; its half width is only about 20 MeV/c. This is much narrower than typical in breakup reactions, where the r.m.s. width is of the order of 250 MeV/c. Once again we emphasize that the longitudinal momentum distribution has very little to do with the momentum content of the bound neutrons; past success of models of the momentum distribution relying on the intrinsic momentum in the initial state may be fortuitous.

5. Angular distribution of neutrons

Having calculated the dipole matrix elements we can now construct the angular distribution of the two neutrons emitted in (^{11}Li, ^{9}Li) reactions that are induced by the Coulomb field. We shall calculate the angular distribution in the rest frame of

^{11}Li and assume that the target moves on the trajectory $(b, 0, vt)$ with an impact parameter b in the x-direction and the velocity v in the z-direction. The angular distributions will be given as functions of the polar angles $(\theta_1, \phi_1; \theta_2, \phi_2)$ with respect to this coordinate system, see fig. 7. A detailed comparison to data requires that the direction of the outgoing ^{9}Li fragment is also measured and used to determine the reaction plane (the xz plane).

We shall formulate the problem for any multipolarity (λ, μ) of the Coulomb field but we shall only apply the general expression to dipole excitations, which we discuss in more detail in subsect. 5.1. The amplitude for emitting the two neutrons with definite momenta $\boldsymbol{k}_1$ and $\boldsymbol{k}_2$ and definite spins can be constructed as a product of three factors; the first is due to the dynamical Coulomb excitation, the second specifies the angle and spin dependence of the emitted neutrons, and the third is a phase shift factor associated with the final state. We shall now describe this construction.

The Coulomb excitation amplitude for a given final state, $f = (k_1 l_1 j_1, k_2 l_2 j_2)$, and impact parameter b, can be obtained from eq. (2.15) of ref. [16]),

$$a_f^{\lambda\mu}(b) = -i\frac{Z_T e}{\hbar v \gamma}\left(\frac{\omega}{c}\right)^{\lambda}\sqrt{2\lambda+1}\, G_{E\lambda\mu}(-1)^{\mu} K_{\mu}(\xi(b)) M_f(E\lambda)\,, \tag{5.1}$$

where $\xi(b) = \omega b/(\gamma v)$ is the so-called adiabaticity parameter, $\hbar\omega = e_1 + e_2 - \varepsilon_{g.s.}$ is the excitation energy, and $M_f(E\lambda)$ is the multipole matrix element to a given final state. This expression was derived for a straight-line trajectory, and the coefficients $G_{E\lambda\mu}$ are given in appendix B of ref. [16]).

The angle and spin dependence of the two-particle wave function can be obtained in the helicity representation from eqs. (A.8) and (A.9) of ref. [6]),

$$D^{\lambda\mu}_{h_1 h_2}(\hat{\boldsymbol{k}}_1, \hat{\boldsymbol{k}}_2) = \frac{1}{8\pi}\sqrt{(2j_1+1)(2j_2+1)}\,\alpha(l_1 j_1 h_1)\alpha(l_2 j_2 h_2)$$
$$\times \sum_{m_1 m_2} \langle j_1 m_1 j_2 m_2 | \lambda\mu\rangle D^{j_1}_{m_1 h_1}(\hat{\boldsymbol{k}}_1) D^{j_2}_{m_2 h_2}(\hat{\boldsymbol{k}}_2)\,. \tag{5.2}$$

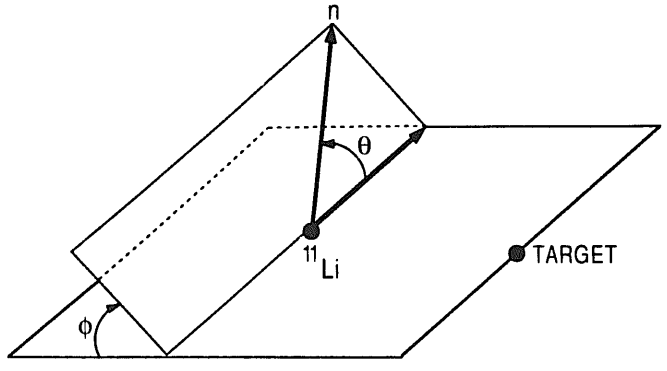

Fig. 7. Illustration of the angles specifying the direction of a neutron emitted in the rest frame of ^{11}Li. The θ-angle is with respect to the beam direction and the ϕ-angle is with respect to the reaction plane.

Here we have suppressed a subscript $(l_1 j_1 l_2 j_2)$ for simplicity, and used the definition $\alpha(ljh) = (-1)^{(h+1/2)(j-l-1/2)}$. The two-particle D-functions (5.2) transform like a tensor of rank λ. They obey other useful relations that we shall make use of, see the appendices C and D.

The last factor we need is the phase shift factor, $\exp(i\delta_f)$, where δ_f is the sum of the phase shifts of the two neutrons in their final state. The amplitude for emitting the two neutrons with helicities h_1 and h_2 and momenta k_1 and k_2 is then given by

$$F^{\lambda\mu}_{h_1h_2}(b, k_1, k_2) = \sum_{l_1 j_1 l_2 j_2} a_f^{\lambda\mu}(b) \exp(i\delta_f) D^{\lambda\mu}_{h_1h_2}(\hat{k}_1, \hat{k}_2) . \tag{5.3}$$

For calculational purposes it is convenient to rewrite this expression as follows

$$F^{\lambda\mu}_{h_1h_2}(b, k_1, k_2) = -i\frac{Z_T e}{\hbar v\gamma}\left(\frac{\omega}{c}\right)^{\lambda} \sqrt{2\lambda+1}\, G_{E\lambda\mu}(-1)^{\mu} \times K_{\mu}(\xi(b)) f^{\lambda\mu}_{h_1h_2}(k_1, k_2) , \tag{5.4}$$

where

$$f^{\lambda\mu}_{h_1h_2}(k_1, k_2) = \sum_{l_1 j_1 l_2 j_2} M_f(E\lambda) \exp(i\delta_f) D^{\lambda\mu}_{h_1h_2}(\hat{k}_1, \hat{k}_2) . \tag{5.5}$$

The amplitudes (5.5) must be antisymmetric with respect to an interchange of the momenta and spins of the two neutrons, i.e.

$$f^{\lambda\mu}_{h_1h_2}(k_1, k_2) = -f^{\lambda\mu}_{h_2h_1}(k_2, k_1) . \tag{5.6}$$

This property follows when the multipole matrix elements are calculated to antisymmetric final states (the isospin part is symmetric).

The differential cross section can now be obtained from an integration over all impact parameters larger than R, where R characterizes the onset of absorption (we have used $R = 1.2(A_P^{1/3} + A_T^{1/3})$), and summing over the possible helicities,

$$\frac{d\sigma^{Cou}}{dk_1\, d\Omega_1\, dk_2\, d\Omega_2} = \sum_{h_1h_2} \int_R^{\infty} 2\pi b\, db \left| \sum_{\lambda\mu} F^{\lambda\mu}_{h_1h_2}(b, k_1, k_2) \right|^2$$

$$= \left(\frac{Z_T e}{\hbar c}\right)^2 \sum_{\lambda\mu\lambda'\mu'} \left(\frac{\omega}{c}\right)^{\lambda+\lambda'-2} \sqrt{(2\lambda+1)(2\lambda'+1)}\, (-1)^{\mu+\mu'} \times (G_{E\lambda\mu})^* G_{E\lambda'\mu'} \sum_{h_1h_2} (f^{\lambda\mu}_{h_1h_2}(k_1, k_2))^* f^{\lambda'\mu'}_{h_1h_2}(k_1, k_2)) g_{\mu\mu'} , \tag{5.7}$$

where

$$g_{\mu\mu'}(\xi(R)) = 2\pi \int_{\xi(R)}^{\infty} \xi\, d\xi\, K_{\mu}(\xi) K_{\mu'}(\xi) , \qquad \xi(R) = \frac{\omega R}{\gamma v} . \tag{5.8}$$

It is useful to check the angle-integrated cross section. From the orthogonality relation (C.7) of the two-particle D-functions one obtains a sum that is diagonal

both in $(\lambda\mu)$ and in the final states,

$$\frac{d\sigma^{\mathrm{Cou}}}{dk_1\,dk_2}=\left(\frac{Z_T e}{\hbar c}\right)^2\left(\frac{\omega}{c}\right)^{2(\lambda-1)}(2\lambda+1)\sum_{l_1 j_1 l_2 j_2}|M_f(E\lambda)|^2 \times\sum_{\lambda\mu}|G_{E\lambda\mu}|^2 g_{\mu\mu}(\xi(R))\,. \tag{5.9}$$

This expression is consistent with eq. (3.1) of ref. [16]), since $(2\lambda+1)$ times the square of the matrix element is identical to the B-value.

Let us mention that in all of our calculations we have used the improved adiabaticity parameter,

$$\xi(R)=\frac{\omega R_{\mathrm{eff}}}{\gamma v},\qquad R_{\mathrm{eff}}=R+\frac{\pi}{2}\frac{Z_P Z_T e^2}{m_0 v^2\gamma}. \tag{5.10}$$

It includes a classical correction term that becomes important at lower velocities [cf. ref. [16])] eq. (2.24)). The correction term originates from the fact that the Coulomb orbits for grazing collisions start to deviate from straight-line trajectories at low velocities. The correction term is not very large in the present context; it is less than 10% for 30 MeV/u ^{11}Li on a lead target.

5.1. SIMPLIFYING FEATURES FOR DIPOLE EXCITATIONS

We shall here study in more detail the angular distribution generated by dipole excitations. It can be calculated directly from eq. (5.7) when one inserts the values [cf. appendix B of ref. [16])]

$$G_{E1,0}=-i\frac{\sqrt{16\pi}}{3}\frac{c}{\gamma v},\qquad G_{E1,1}=-G_{E1,-1}=\frac{\sqrt{8\pi}}{3}\frac{c}{v}. \tag{5.11}$$

There are, however, several simplifying features that we want to point out and which may help us to better understand the calculated angular distributions.

First of all, it turns out that the interference between the longitudinal ($\mu=0$) and the transverse amplitudes ($\mu=\pm1$) vanishes. This is demonstrated in appendix D. Without the interference term we now obtain the following expression for the angular distribution generated by dipole excitations,

$$\frac{d\sigma^{\mathrm{Dip}}}{dk_1\,d\Omega_1\,dk_2\,d\Omega_2}=\left(\frac{4\pi Z_T e}{3\hbar v}\right)^2 \times\frac{3}{\pi}\sum_{h_1 h_2}\left(\frac{1}{\gamma^2}|f^{10}_{h_1 h_2}|^2 g_{00}(\xi)+\tfrac{1}{2}|f^{11}_{h_1 h_2}-f^{1-1}_{h_1 h_2}|^2 g_{11}(\xi)\right). \tag{5.12}$$

The g-functions are defined in (5.8), and they are here given by

$$g_{00}(\xi)=\pi\xi^2(K_1^2(\xi)-K_0^2(\xi))\,, \tag{5.13a}$$

$$g_{11}(\xi)=\pi\xi^2\left(K_0^2(\xi)-K_1^2(\xi)+\frac{2}{\xi}K_0(\xi)K_1(\xi)\right). \tag{5.13b}$$

A further simplification in the discussion of the angular distribution (5.12) is that the shape of the longitudinal part ($\mu = 0$) is identical to that of the transverse part ($\mu = \pm 1$) when one calculates them with respect to their respective symmetry axes. Moreover, each component is invariant under rotations around its symmetry axis. The symmetry axis for the longitudinal part is the beam direction (the z-axis), whereas the transverse part has its symmetry axis along the total momentum transfer to the ^{11}Li nucleus (the x-axis). These properties follow from the fact that the f-amplitudes (5.5) transform like a tensor. Thus if one performs a rotation of 90° around the y-axis, the longitudinal amplitudes $f^{10}_{h_1h_2}$ will transform into the transverse amplitudes $\sqrt{\frac{1}{2}}(f^{11}_{h_1h_2} - f^{1-1}_{h_1h_2})$. In the next section we shall therefore only illustrate the shape of one of two components. The great advantage is that we can present results which are independent of the beam energy.

Let us finally discuss the single-neutron angular distribution. The basic integration over the orientation of the second neutron has been performed in appendix C. The distribution has only two contributions for dipole excitations, a spherical part and a quadrupole term. It is therefore clear that the longitudinal (L) component must have the form,

$$\left(\frac{\mathrm{d}\sigma^{\mathrm{Dip}}}{\mathrm{d}k_1\,\mathrm{d}\Omega_1\,\mathrm{d}k_2}\right)_L = \left(\frac{\mathrm{d}\sigma^{\mathrm{Dip}}}{\mathrm{d}k_1\,\mathrm{d}k_2}\right)_L \frac{1}{4\pi}(1 + a_1(k_1, k_2)P_2(\cos\theta_1))\,, \tag{5.14}$$

since it is invariant under rotations around the z-axis. Using the results given in appendix C one can derive the following expression for the anisotropy,

$$a_i(k_1, k_2) = \sum_{l_1 j_1 l_2 j_2} \sum_{l_1' j_1'} M_f^*(\mathrm{E1}) M_{f'}(\mathrm{E1}) \exp\left(i(\delta_{f'} - \delta_f)\right) \times C_{20}^{1010}(j_1 j_1'; j_2) \Big/ \sum_{l_1 j_1 l_2 j_2} |M_f(\mathrm{E1})|^2\,. \tag{5.15}$$

The C-coefficients are given in eq. (C.6). The first sum is over the (l, j) quantum numbers of the two final states f and f'; they may differ for the first particle but they are identical for the second particle. The single-neutron angular distribution is discussed in further detail in subsect. 6.1.

6. Results on angular distributions

We now discuss the two-particle angular distribution (5.12) in the final state of the ^{11}Li nucleus. Our initial expectation was that the correlation function would be quite simple, having as a main feature a correlation between the emission directions of the two neutrons in the final state. We found instead that the predicted correlation function depends in an intricate way on the various energy and angular variables of the two neutrons, and does not favor parallel emission of the two neutrons. The general features of the angular distributions are an enhanced emission of the two neutrons when they are emitted on opposite sides of the symmetry axis, and the largest enhancement is observed at the lowest final-state energies.

As mentioned in sect. 5, we can simplify the discussion of the distribution by considering the longitudinal ($\mu = 0$) and the transverse ($\mu = \pm 1$) components individually. The distributions of the two components are identical when referred to the appropriate symmetry axes, and their relative weights depend on the beam velocity. We shall therefore only illustrate the shape of the $\mu = 0$ component,

$$D_{\mu=0}(e_1\theta_1\phi_1; e_2\theta_2\phi_2) = (4\pi)^2 \sum_{l_1 l_2} |f^{10}_{l_1 l_2}(\hat{k}_1, \hat{k}_2)|^2 \Big/ \sum_{l_1 j_1 l_2 j_2} |M_f(\mathrm{E1})|^2 . \qquad (6.1)$$

This is normalized over all directions to an average value of one for given final state energies (e_1, e_2), cf. eqs. (5.5) and (5.12). At large velocities, where the transverse excitations dominate, this distribution will be close to the actual shape of the total angular distribution when the z-axis is chosen along the direction of the total momentum transfer to the ^{11}Li system.

The $\mu = 0$ component is invariant under rotations about the z-axis, so we need only display the angular dependence on three variables: θ_1, θ_2 and the difference $\Delta\phi = \phi_1 - \phi_2$. Moreover, because of reflection symmetry we need only show the distribution for $0° \leq \theta_1 \leq 180°$ and $-90° \leq \theta_2 \leq 90°$ for a given value of $\Delta\phi$. Note that the positive and negative values of θ_2 cover opposite sides of the z-axis. Actually, these angular ranges can be reduced further when the energies of the two emitted particles are identical. This will be visible in the figures as a symmetry under interchange of the two particles.

We first examine the angular distribution at very low excitations. Here, because of the centrifugal barrier, the most important partial waves are s- and p-waves. The $\mu = 0$ amplitude has a simple form in this case,

$$\langle\theta_1\phi_1\theta_2\phi_2|(ps)^{1,0}\rangle \simeq \alpha(\cos\theta_1 + \cos\theta_2)|S=0\rangle + \beta \sum_{m=\pm 1} (\mathrm{e}^{-im\phi_1}\sin\theta_1 - \mathrm{e}^{-im\phi_2}\sin\theta_2)|S=1, m\rangle , \qquad (6.2)$$

where S labels the total spin of the two neutrons. For the $S = 0$ component, particles are emitted with an amplitude proportional to $\cos\theta$ and there is a mild correlation between them along the z-axis. On the other hand, the $S = 1$ components vanish when the particles come out in the same direction; they are enhanced near $\theta \simeq 90°$ with the particles on opposite sides of the z-axis. The coefficients α and β in eq. (6.2) depend on the spin structure of the continuum states. In a pure $(\mathrm{p}_{1/2}\mathrm{s}_{1/2})^{1,0}$ configuration $\alpha = \sqrt{2}\,\beta$, while the $(\mathrm{p}_{3/2}\mathrm{s}_{1/2})^{1,0}$ configuration has $\alpha = -2\sqrt{2}\,\beta$.

The general features of (6.2) are indeed observed in the calculated distributions at low excitations when we ignore the effect of the final state interaction. A typical example is shown in fig. 8 for the final state neutron energies $e_1 = e_2 = 0.1$ MeV. This corresponds to an excitation energy of 0.4 MeV. The two particles are fixed to be on either the same side ($\Delta\phi = 0$) or on the opposite side ($\Delta\phi = 180°$) of the z-axis, the latter case being represented by negative values of θ_2. The figure shows a moderately strong positive correlation between the two particles, as expected from a preponderance of $S = 0$ in the correlated neutron pair. The distribution is in

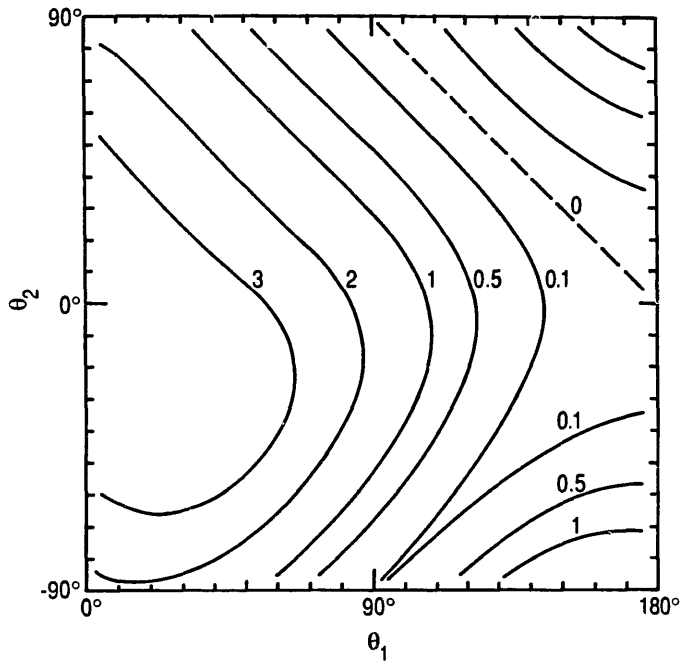

Fig. 8. Angular distribution of the two valence neutrons emitted in the rest frame of ^{11}Li, with energies $e_1 = e_2 = 0.1$ MeV and $\Delta\phi = 0$. Only the $\mu = 0$ component (6.1) is shown, and the pair-interaction in the final state has been set to zero. The contour plot is shown as a function of the angles of the two neutrons with respect to the symmetry axis.

reasonable agreement with eq. (6.2) if we choose the parameters $\alpha \gg \beta$. This corresponds to a coherent mixture of $(p_{1/2}s_{1/2})$ and $(p_{3/2}s_{1/2})$ final states, populated with about the same strength. It might be thought that the $(p_{1/2}s_{1/2})$ continuum state would give the dominant contribution at low excitations because $p^2_{1/2}$ states constitute about 77% of the ground state [6]). However, we find that the $(p_{3/2}s_{1/2})$ final state is almost as important; it arises from the much weaker $p^2_{3/2}$ and $s^2_{1/2}$ components of the ground state.

When we include the pair interaction in the final state, the overall preference for an anticorrelation between the two neutrons becomes a characteristic feature. This is illustrated in fig. 9, which in all other respects was obtained for the same conditions that was used in fig. 8. The effect of the final-state interaction is to populate single-particle states of higher orbital angular momenta and the simple parameterization (6.2) no longer holds. It is seen that the maximum of the distribution is now located at $\theta_1 = -\theta_2 = 55°$. It has also seen that the distribution is zero for $\theta_1 + \theta_2 = 180°$. This is a special feature for $\Delta\phi = 0°$ and $e_1 = e_2$.

The angular distribution becomes more complicated at higher excitation energy, as single-particle states of higher orbital momenta become populated. The (dp) amplitude becomes important at several hundred keV excitation energy. It interferes destructively with the (ps) amplitude when both particles are emitted along the symmetry axis. This behavior is contrary to the usual constructive interference for correlated particles when amplitudes are added, causing us initially to doubt the

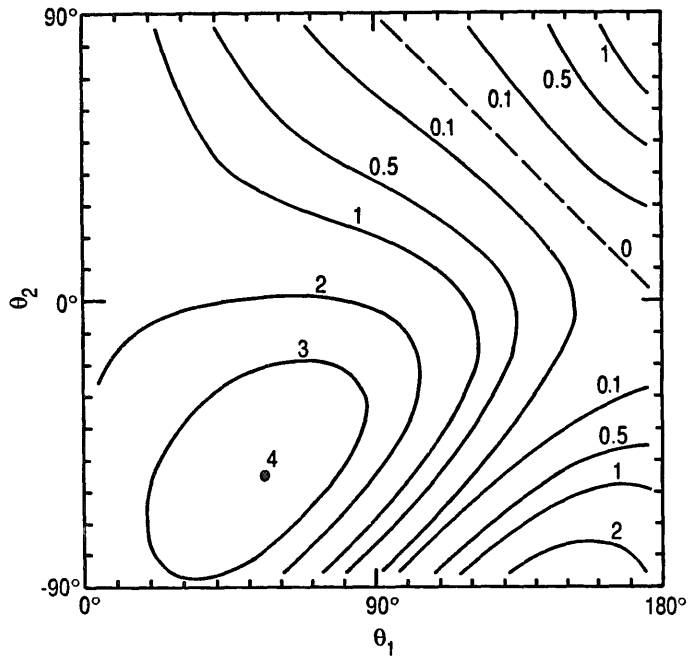

Fig. 9. Angular distribution of the two valence neutrons emitted in the rest frame of ^{11}Li, with energies $e_1 = e_2 = 0.1$ MeV and $\Delta\phi = 0$. Only the $\mu = 0$ component (6.1) is shown. The effect of the pair-interaction in the final state has been included. The contour plot is shown as a function of the angles of the two neutrons with respect to the symmetry axis.

consistency of our phase conventions. However, the anticorrelation does follow from simple considerations about the wave function of the dipole state. When the dipole operator is applied to the p-state of the ground-state wave function, it produces d- and s-components which interfere constructively on the z-axis outside the nuclear surface. Projecting this onto momentum states, the i^l factor in the angular decomposition of a plane wave reverses the phase relation to put the maximum at 90°.

Fig. 10 shows the angular distribution at an excitation energy of 1.2 MeV and $\Delta\phi = 0°$, 180°. The two neutrons have the same energy, $e_1 = e_2 = 0.5$ MeV, in the left panel of fig. 10. With more partial waves, the emission in the direction of the symmetry axis has now become suppressed. The peak in the distribution appears more like a ridge, with the largest maximum for an opening angle of 80° between the two particles. The right panel of fig. 10 shows the effect of changing the energies of the two particles away from the symmetric $e_1 = e_2$ case.

Some of the angular distributions shown in figs. 8-10 have a rather complicated dependence on $\theta_1 - \theta_2$. The dependence on $\theta_1 + \theta_2$, on the other hand, is much simpler; it is generally of the form: $A + B\cos(\theta_1 + \theta_2 + \delta)$. This is a characteristic feature for dipole excitations and it follows for the fact that the f-amplitudes (5.5) in this case transform like a tensor of rank unity. In particular, when the energies of the two emitted neutrons are identical and $\Delta\phi = 0$, the dependence on $\theta_1 + \theta_2$ reduces to an even simpler form: $B\cos(\theta_1 + \theta_2)$, which vanishes for $\theta_1 + \theta_2 = 180°$, cf. figs. 8-10.

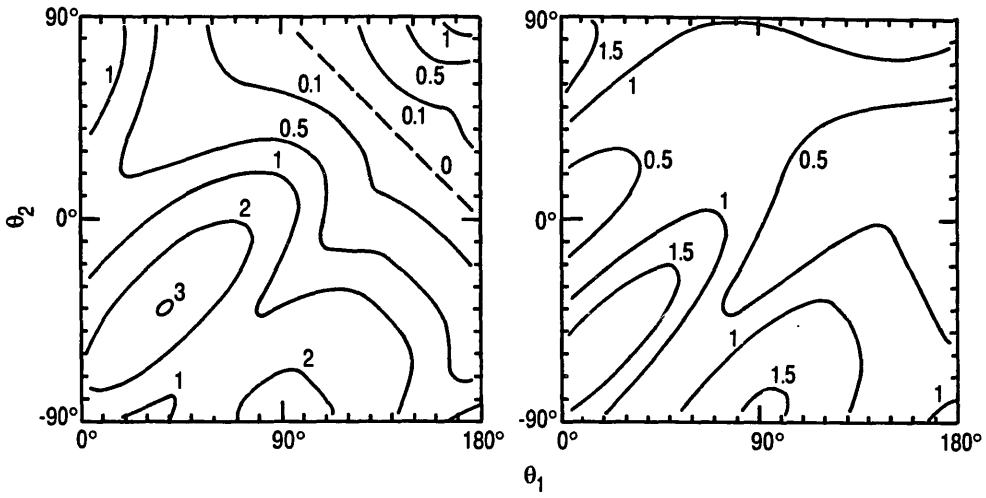

Fig. 10. Similar to fig. 9 but for $e_1 = e_2 = 0.5$ MeV (left panel) and $e_1 = 0.25$ and $e_2 = 0.75$ MeV (right panel).

No data is available on the two-neutron angular distributions, but the needed experiments are now in progress [21]). As mentioned in sect. 4, data exists for partially integrated distributions, in particular single-neutron angular distributions and recoil momentum distributions. In sect. 4 we examined the recoil momentum distribution of the residual ^{9}Li nucleus neglecting the effect of correlations. To see how good an approximation that is, we evaluated the expectation of the total momentum of the neutron pair for the conditions of fig. 10, i.e. an excitation energy of 1.2 MeV. At 70 MeV/u, we find that the total longitudinal momentum is reduced by roughly 20% with respect to an uncorrelated emission. Thus, the correction for correlations is rather small.

6.1. ONE-NEUTRON ANGULAR DISTRIBUTIONS

The most obvious partially integrated observable is the single-neutron angular distribution, which was calculated by one of us [19]) in the independent particle model. The angular distribution has again two components, a longitudinal (L) and a transverse (T). In the rest frame of the ^{11}Li nucleus each of them must have the form $1 + aP_2(\cos\theta)$, where θ is the azimuthal angle with respect to the relevant symmetry axis, and a is the same for both directions for given final-state energies of the two neutrons. It is therefore easy to derive the general expression for the differential cross section in a coordinate system where the z-axis is identical to the beam direction,

$$4\pi \frac{\mathrm{d}\sigma^{\mathrm{Dip}}}{\mathrm{d}k_1\,\mathrm{d}\Omega_1\,\mathrm{d}k_2} = \frac{\mathrm{d}\sigma^{\mathrm{Dip}}}{\mathrm{d}k_1\,\mathrm{d}k_2} + aP_2(\cos\theta_1)\left(\left(\frac{\mathrm{d}\sigma^{\mathrm{Dip}}}{\mathrm{d}k_1\,\mathrm{d}k_2}\right)_L - \frac{1}{2}\left(\frac{\mathrm{d}\sigma^{\mathrm{Dip}}}{\mathrm{d}k_1\,\mathrm{d}k_2}\right)_T\right)$$
$$+ a\tfrac{3}{4}\sin^2\theta_1\cos(2\phi)\left(\frac{\mathrm{d}\sigma^{\mathrm{Dip}}}{\mathrm{d}k_1\,\mathrm{d}k_2}\right)_T . \qquad (6.3)$$

An analytic expression for the anisotropy in terms of the dipole matrix elements is given in eq. (5.15). Typical values for $e_1 = e_2 < 0.4$ MeV are $a \approx 0.4$.

In a singles experiment, such as reported in ref. [4]), the reaction plane is not measured and the last term in eq. (6.3) drops out. The effective anisotropy is then much reduced due to a partial cancellation of the longitudinal and transverse components. At the beam energy of 29 MeV/u one finds that the effective anisotropy is reduced to $a_{\text{eff}} \approx -0.1$ for $e_1 = e_2 = 0.1$. It is therefore reasonable in this case to assume that the distribution is spherical in the rest frame of ^{11}Li, as we did for our crude estimate in sect. 4. To observe the interesting anisotropy in eq. (6.3) would require detecting the residual nucleus as well, so that the momentum vectors in the ^{11}Li frame could be reconstructed.

7. Conclusions

We presented a fully selfconsistent three-particle model of the ground state of ^{11}Li and its response to Coulomb excitation. With the model, we could assess the importance of correlations and of shell physics in the structure of weakly bound nuclei. Superficially the independent-particle shell model is remarkably accommodating, since it reproduces the ground-state density quite accurately when a suitable binding energy prescription is used to construct the single-particle wave functions. Also, the shape of the dipole strength function is rather well described in this framework. This model has a long history as the direct mechanism for the inverse capture process. However, the correlations reveal themselves in the total strength of the dipole excitation, enhancing it by 50% in ^{11}Li. In ordinary nuclei correlations also affect the dipole strength, but there it is particle-hole correlations that are important and their effect is to decrease the strength, shifting it to higher excitation energies.

There are other aspects of shell structure that are observable in the final state. The dipole response, calculated as a differential in the kinetic energy of the two emitted neutrons, exhibits an interesting ridge structure at higher excitations. If the energy of one of the emitted neutrons is large then the most likely energy of the second neutron is close to the energy of the resonant state in ^{10}Li. This feature clearly reflects the shell structure of ^{10}Li. It disappears when we use free-particle states as final states. We mention in this connection that there are some uncertainties in the knowledge of the shell structure of ^{10}Li. We have adjusted our single-particle hamiltonian to reproduce the measured neutron resonance [22]) at 800 keV. Recent measurements [23]), however, suggest a much smaller value of 150 ± 150 keV. It would be very useful if the experimental uncertainty on this point could be resolved, since the structure of ^{10}Li is an important input to our model.

The angular distribution of neutrons emitted in Coulomb induced reactions has two components: a longitudinal and a transverse. The transverse component dominates in (^{11}Li, ^{9}Li) reactions at intermediate and high energies, and it is axially

symmetric around the direction of the total momentum transfer. The longitudinal component has the same shape but its symmetry axis is along the beam direction. The angular correlation has a complex behavior depending on both the shell structure and the interaction between the neutrons. The most striking feature of our calculations is actually an anticorrelation; the preferred emission is with the two neutrons on opposite sides of the symmetry axis and with a rather large opening angle. This is contrary to what one would expect in a naive dineutron model. Only at very low excitations one may observe the two neutrons coming out in the same direction with a larger than average probability but even here the anticorrelated emission is the most likely, with an opening angle of about 110°. Measurements are clearly needed to test and constrain possible models.

It is common to interpret the momentum distribution in breakup reactions as a measure of the momentum in the initial wave function. Our model can be used to test the validity of this identification. The momentum distribution of dipole excitation is similar to the ground-state momentum distribution, since the dipole operator does not change the momentum content much. It was easy to compute the momentum distribution of the dipole excitation by taking free-particle states, i.e. plane waves, for the neutrons in the final state. This gave a similar total strength as in the fully correlated response but the average excitation energy was too high by about 50%. The higher momentum components in the wave function are not observed in the final state because they are only present in regions where the particles are interacting with other nucleons.

Our model reproduces the integrated cross section that has been extracted from data. However, the extracted values are model-dependent because the nuclear breakup must be subtracted from the observed cross section. It would therefore be useful to calculate the nuclear part of the reaction within the same model we used to calculate the dipole response.

A further success of our model, and one that supports the existence of a concentration of strength at low excitation, is the single-neutron angular distributions that has recently been measured [4]). The data show a strong narrow peak at forward angles, whereas reactions with more tightly bound nuclei yield a much broader distribution. A similar behavior is expected for the recoil momentum distribution, but here the comparison with experiment is less satisfying. The transverse recoil momentum is obscured on a heavy target due to the Coulomb deflection. The observed narrowness of the recoil momentum peak on a light target is more extreme than we might expect. Hopefully, this issue will be clarified by measurements of the longitudinal recoil momentum.

From a technical aspect, the two-particle Green function proved very practical for calculating the two-particle continuum. In fact, without it the calculation would not have been feasible. The technique of ref. [6]) needed only to be refined by using principle value integration rather than a sum over discrete states. Other methods, such as the Fadeev equations, may be more powerful for dealing with realistic

nucleon-nucleon interactions in a bound state context, but we do not know of any computational tractable application to the two-particle continuum.

This work was supported by the U.S. Department of Energy, Nuclear Physics Division under contract no. W-31-109-ENG-38, and by the National Science Foundation under grant no. PHY 90-17077.

Appendix A

CONTINUUM GREEN'S FUNCTION

We describe here the calculation of the local, noninteracting two-particle Green function associated with the dipole response. It can be obtained from the two-particle wave functions (A.11) of ref. [6]). This Green function, used in connection with the pair interaction, is subject to the constraint that the two-particle energies must be smaller than the cutoff $E_c = (\hbar k_c)^2/2m$. Here we assume for simplicity that all single-particle states belong to the continuum, which is the case for ^{11}Li. Then the local Green function is,

$$G(E, \boldsymbol{r}, \boldsymbol{r}') = \sum_{l_1 j_1 l_2 j_2 M} \frac{2j_1+1}{8\pi} (j_1 \tfrac{1}{2} 10 | j_2 \tfrac{1}{2})^2 \frac{2m}{\hbar^2} g_2(E, r, r')\, Y_{1M}(\hat{\boldsymbol{r}})\, Y^*_{1M}(\hat{\boldsymbol{r}}'), \quad \text{(A.1)}$$

where

$$g_2(E, r, r') = \int_0^{k_c} \mathrm{d}k_1 \int_0^{\sqrt{k_c^2 - k_1^2}} \mathrm{d}k_2 \frac{\phi_{k_1 l_1 j_1}(r)\phi_{k_2 l_2 j_2}(r)\phi_{k_1 l_1 j_1}(r')\phi_{k_2 l_2 j_2}(r')}{k_1^2 + k_2^2 - k_E^2 - i\eta}, \quad \text{(A.2)}$$

and $E = (\hbar k_E)^2/2m$ is the total energy of the final state. The continuum single-particle wave functions are here normalized to the asymptotic form,

$$\phi_{klj} = \sqrt{\frac{2}{\pi}} \frac{\sin(kr + \delta)}{r}. \quad \text{(A.3)}$$

Difficulties arise in the numerical calculation of the real part of g_2 due to the presence of poles in the integrand. In a discrete basis the poles will cause a strong energy dependence near the poles. However, when all states belong to the continuum, one should expect a smooth dependence on energy. One can overcome this difficulty by using Gauss-Legendre integration. To see this let us first substitute $k_1 = k \cos(\theta)$ and $k_2 = k \sin(\theta)$ and white,

$$g_2(E, r, r') = \int_0^{k_c} \mathrm{d}k\, k \frac{\rho_2(k, r, r')}{k^2 - k_E^2 - i\eta}, \quad \text{(A.4)}$$

where

$$\rho_2(k, r, r') = \int_0^{\pi/2} \mathrm{d}\theta\, \phi_{k_1}(r)\phi_{k_2}(r)\phi_{k_1}(r')\phi_{k_2}(r'). \quad \text{(A.5)}$$

The function ρ_2 is a smooth function of k, and we only need to know it for $0 \leq k \leq k_c$. Transforming to the variable $x = 2k/k_c - 1$ we can therefore expand ρ_2 on Legendre polynomials,

$$\rho_2(k, r, r') = \sum_n \rho_2(n, r, r') P_n(x) , \tag{A.6}$$

where

$$\rho_2(n, r, r') = \frac{2n+1}{2} \int_{-1}^{1} \mathrm{d}x \, P_n(x) \rho_2(k = k_c \tfrac{1}{2}(x+1), r, r') . \tag{A.6'}$$

Inserting eq. (A.6) into (A.4) we can now perform the principal value integration analytically,

$$\mathrm{Re}\,(g_2(E, r, r')) = -\sum_n \rho_2(n, r, r')(Q_n(x_E) + Q_n(-(2+x_E)) , \tag{A.7}$$

where Q_n are Legendre polynomials of the second kind, and $x_E = 2k_E/k_c - 1$. The expression for the imaginary part, on the other hand, is much simpler,

$$\mathrm{Im}\,(g_2(E, r, r')) = \tfrac{1}{2}\pi \rho_2(k_E, r, r') . \tag{A.8}$$

Appendix B

CALCULATION OF $G_D(E, r)$

We can perform the calculation of $G_D(E, r)$, defined in eq. (3.13), in the same way we calculated the local two-particle Green function in appendix A. Thus, using the expression (A.11) of ref.[6]) for the local two-particle states, we obtain

$$G_D(E, r) = \sum_{l_1 j_1 l_2 j_2 \mu} (-1)^{l_1} \sqrt{\frac{2j_1+1}{8\pi}} \langle j_1 \tfrac{1}{2} 10 | j_2 \tfrac{1}{2} \rangle \frac{2m}{\hbar^2} g_D(E, r) Y_{1\mu}(\hat{r}) , \tag{B.1}$$

where

$$g_D(E, r) = \int_0^{k_c} \mathrm{d}k_1 \int_0^{\sqrt{k_c^2 - k_1^2}} \mathrm{d}k_2 \frac{\phi_{k_1 l_1 j_1}(r) \phi_{k_2 l_2 j_2}(r)}{k_1^2 + k_2^2 - k_E^2 - i\eta} \langle (j_1 j_2)_\mu^1 | D_\mu(r_1, r_2) | \Psi_{\mathrm{g.s.}} \rangle , \tag{B.2}$$

and $E = (\hbar k_E)^2/2m$. The continuum single-particle wave functions are here normalized according to eq. (A.3).

The dipole matrix elements in (B.2) are similar to that given in eq. (3.1), and they are evaluated for final states with the quantum numbers $(k_1 l_1 j_1; k_2 l_2 j_2)$. As in appendix A we now substitute $k_1 = k \cos(\theta)$ and $k_2 = k \sin(\theta)$ and write,

$$g_D(E, r) = \int_0^{k_c} \mathrm{d}k \, k \frac{\rho_D(k, r)}{k^2 - k_E^2 - i\eta} , \tag{B.3}$$

where

$$\rho_D(k, r) = \int_0^{\pi/2} \mathrm{d}\theta \, \phi_{k_1}(r) \phi_{k_2}(r) \langle (j_1 j_2)_\mu^1 | D_\mu(r_1, r_2) | \Psi_{\mathrm{g.s.}} \rangle . \tag{B.4}$$

The latter expression is expanded on Legendre polynomials,

$$\rho_D(k, r) = \sum_n \rho_D(n, r) P_n(x) , \tag{B.5}$$

where $x = 2k/k_c - 1$. We can now perform the integration in (B.3) analytically. The results for the real and the imaginary parts are similar to those given in eqs. (A.7) and (A.8), respectively.

Appendix C

BASIC ANGLE INTEGRALS

In order to derive an expression for the single-neutron angular distribution one has to perform the following integral

$$I^{\lambda\lambda'}_{\mu\mu'}(\hat{k}_1) = \sum_{h_1 h_2} \int d\Omega_2 \, (D^{\lambda\mu}_{h_1 h_2}(\hat{k}_1, \hat{k}_2))^* D^{\lambda'\mu'}_{h_1 h_2}(\hat{k}_1, \hat{k}_2) , \tag{C.1}$$

where the two-particle D-functions are defined in eq. (5.2). From the orthogonality properties of the standard single-particle D-functions we obtain

$$I^{\lambda\lambda'}_{\mu\mu'}(\hat{k}_1) = \delta_{l_2 l_2'} \delta_{j_2 j_2'} \frac{1}{8\pi} \sqrt{(2j_1+1)(2j_1'+1)} \sum_{m_1 m_2 m_1'} \langle j_1 m_1 j_2 m_2 | \lambda\mu \rangle$$
$$\times \langle j_1' m_1' j_2 m_2 | \lambda'\mu' \rangle \sum_h \alpha(l_1 j_1 h) \alpha(l_1' j_1' h) (D^{j_1}_{m_1 h}(\hat{k}_1))^* D^{j_1'}_{m_1' h}(\hat{k}_1) . \tag{C.2}$$

The product of the latter two D-functions can be decomposed as follows

$$(D^{j_1}_{m_1 h})^* D^{j_1'}_{m_1' h} = \sum_{IM} \frac{2I+1}{2j_1'+1} \langle j_1 m_1 I M | j_1' m_1' \rangle \langle j_1 h I 0 | j_1' h \rangle (D^I_{M0})^* . \tag{C.3}$$

We can now perform the summation over helicity, which involves

$$\sum_h \alpha(l_1 j_1 h) \alpha(l_1' j_1' h) \langle j_1 h I 0 | j_1' h \rangle$$
$$= (-1)^{j_1 + j_1' - 1} \langle j_1 \tfrac{1}{2} I 0 | j_1' \tfrac{1}{2} \rangle ((-1)^{l_1 + l_1'} + (-1)^I) . \tag{C.4}$$

Inserting eqs. (C.3), (C.4), into (C.2) we now obtain

$$I^{\lambda\lambda'}_{\mu\mu'}(\hat{k}_1) = \delta_{l_2 l_2'} \delta_{j_2 j_2'} \frac{1}{4\pi} \sum_{IM} (D^I_{M0}(\hat{k}_1))^* C^{\lambda\mu\lambda'\mu'}_{IM}(j_1 j_1'; j_2) , \tag{C.5}$$

where

$$C^{\lambda\mu\lambda'\mu'}_{IM}(j_1 j_1'; j_2)$$
$$= (-1)^{j_1 + j_1' - 1} (2I+1) \sqrt{\frac{2j_1+1}{2j_1'+1}} \tfrac{1}{2} ((-1)^{l_1 + l_1'} + (-1)^I) \langle j_1 \tfrac{1}{2} I 0 | j_1' \tfrac{1}{2} \rangle$$
$$\times \sum_{m_1 m_2 m_1'} \langle j_1 m_1 I M | j_1' m_1' \rangle \langle j_1 m_1 j_2 m_2 | \lambda\mu \rangle \langle j_1' m_1' j_2 m_2 | \lambda'\mu' \rangle . \tag{C.6}$$

Note that a non-zero value of the C-coefficients requires that $M = \mu' - \mu$. We find it useful to give these general expressions but we shall only use them for dipole excitations. In this case the sum (C.5) includes only two values of I, viz. $I = 0$ and 2.

Finally, integrating over all orientations of the first neutron we obtain the normalization,

$$\int \mathrm{d}\Omega_1 \, I^{\lambda\lambda'}_{\mu\mu'}(\hat{\boldsymbol{k}}_1) = \delta_{l_1 l_1'}\delta_{j_1 j_1'} C^{\lambda\mu\lambda'\mu'}_{00} = \delta_{l_1 l_1'}\delta_{j_1 j_1'}\delta_{l_2 l_2'}\delta_{j_2 j_2'}\delta_{\lambda\lambda'}\delta_{\mu\mu'} . \tag{C.7}$$

Appendix D

LONGITUDINAL-TRANSVERSE INTERFERENCE

The angular distribution (5.7) simplifies considerably for dipole excitations. Here we demonstrate that the interference between the longitudinal ($\mu = 0$) and the transverse ($\mu = \pm 1$) amplitudes vanishes. This is not obvious at first glance since the dipole matrix elements can be complex. Inserting eq. (5.11) into (5.7) we see that the interference term is proportional to

$$\mathrm{Im} \sum_{h_1 h_2} (f^{10}_{h_1 h_2})^* (f^{11}_{h_1 h_2} - f^{1-1}_{h_1 h_2}) . \tag{D.1}$$

Inserting now the expression (5.5) for the f-amplitudes one finds that the interference term vanishes if

$$\mathrm{Im} \sum_{h_1 h_2} (D^{10}_{h_1 h_2})^* (D^{11}_{h_1 h_2} - D^{1-1}_{h_1 h_2}) = 0 . \tag{D.2}$$

This relation, on the other hand, is a consequence of the following general property of the two-particle D-functions,

$$(D^{\lambda\mu}_{h_1 h_2})^* = -(-1)^{\mu - h_1 - h_2}(-1)^{l_1 + l_2 - \lambda} D^{\lambda\,-\mu}_{-h_1 - h_2} , \tag{D.3}$$

which can be derived from the definition (5.2). The relation (D.3) may also have simplifying consequences for higher multipolarities. Without the interference between the longitudinal and the transverse amplitudes the angular distribution reduces to the simple form given in eq. (5.12).

References

1) I. Tanihata *et al.*, Phys. Rev. Lett. **55** (1985) 2676
2) T. Kobayashi *et al.*, Phys. Rev. Lett. **60** (1988) 2599
3) T. Kobayashi *et al.*, Phys. Lett. **B232** (1989) 51
4) R. Anne *et al.*, Phys. Lett. **B250** (1990) 19
5) T. Kobayashi *et al.*, "Spectroscopy of the exotic nucleus ^{11}Li via pion double charge exchange reaction", (in press);
   B. Blank *et al.*, Z. Phys. **A340** (1991) 41
6) G.F. Bertsch and H. Esbensen, Ann. of Phys. **209** (1991) 327

7) T. Hoshino, H. Sagawa and A. Arima, Nucl. Phys. **A523** (1991) 228
8) A. Hayes, Phys. Lett. **B254** (1991) 15
9) P.G. Hansen and B. Jonson, Europhys. Lett. **4** (1987) 409
10) C. Bertulani, G. Baur and M. Hussein, Nucl. Phys. **A526** (1991) 751
11) L. Johannsen, A.S. Jensen and P.G. Hansen, Phys. Lett. **B244** (1990) 357
12) J. Bang *et al.*, preprint, Niels Bohr Institute NBI-91-31, 1991
13) M. Zhukov *et al.*, Europhys. Lett. **13** (1990) 703
14) G. Bertsch and S.F. Tsai, Phys. Reports **C18** (1975) 127
15) H. Sagawa and M. Honma, Phys. Lett. **B251** (1990) 17
16) A. Winther and K. Alder, Nucl. Phys. **A319** (1979) 518
17) A. Sustich (submitted for publication)
18) G. Bertsch, H. Esbensen and A. Sustich, Phys. Rev. **C42** (1990) 758
19) H. Esbensen, Phys. Rev. **C44** (1991) 440
20) S. Austin, private communication
21) A. Galonsky, private communication
22) J.M. Wilcox *et al.*, Phys. Lett. **B59** (1975) 142
23) A.I. Amelin *et al.*, Sov. J. Nucl. Phys. **52** (1990) 782